Analytica Chimica Acta 1287 (2024) 342047

Contents lists available at ScienceDirect

Analytica Chimica Acta

journal homepage: www.elsevier.com/locate/aca

TiO_2 nanorod arrays@PDA/Ag with biomimetic polydopamine as binary mediators for duplex SERS detection of illegal food dyes

Lin Tan [a,1], Yanqiang Cao [a,1], Juanjuan Yan [a,1], Kang Mao [b], Li Liu [c], Xiaolong Wang [d,**], Weichun Ye [a,*], R.A. Harris [e,***], Hua Zhang [b,****]

[a] State Key Laboratory of Applied Organic Chemistry, Key Laboratory of Special Functional Materials and Structural Design (Ministry of Education), Lanzhou University, Lanzhou 730000, China
[b] State Key Laboratory of Environmental Geochemistry, Institute of Geochemistry, Chinese Academy of Sciences, Guiyang, 550081, China
[c] Center for Inspection of Gansu Drug Administration (Center for Vaccine Inspection of Gansu), Lanzhou 730030, China
[d] State Key Laboratory of Solid Lubrication, Lanzhou Institute of Chemical Physics, Chinese Academy of Sciences, Lanzhou 730000, China
[e] Department of Physics, University of the Free State, Bloemfontein 9301, South Africa

HIGHLIGHTS

- Biomimetic PDA was introduced to the semiconductor-Ag heterostructures for SERS applications.
- Due to the structural features, PDA served as binary mediators of electron transfer and enrichment.
- DFT was used to analyze the interactions between PDA and dyes to improve the efficient enrichment.
- Individual and simultaneous detection of RhB and CV could be conducted in chili food.

GRAPHICAL ABSTRACT

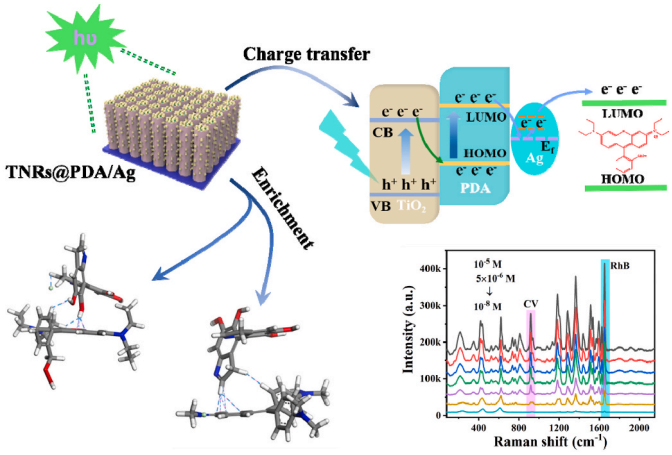

ARTICLE INFO

Handling Editor: Dr. J.P. Landers

Keywords:
Surface-enhanced Raman scattering (SERS)

ABSTRACT

Based on TiO_2 nanorod arrays@PDA/Ag (TNRs@PDA/Ag), a better surface-enhanced Raman scattering (SERS) sensor with effective enrichment and enhancement was investigated for duplex SERS detection of illicit food dyes. Biomimetic PDA functions as binary mediators by utilizing the structural characteristics of polydopamine (PDA), which include the conjugated structure and abundant hydrophilic groups. One PDA functioned as an

* Corresponding author.
** Corresponding author.
*** Corresponding author.
**** Corresponding author.
E-mail addresses: wangxl@licp.cas.cn (X. Wang), yewch@lzu.edu.cn (W. Ye), harrisra@ufs.ac.za (R.A. Harris), zhanghua@mail.gyig.ac.cn (H. Zhang).
[1] They have the same contribution to this paper.

https://doi.org/10.1016/j.aca.2023.342047
Received 15 October 2023; Received in revised form 11 November 2023; Accepted 18 November 2023
Available online 25 November 2023

Polydopamine modification
Duplex detection
Illegal food dyes

electron transfer mediator to enhance the efficiency of electron transfer, and the other as an enrichment mediator to effectively enrich rhodamine B (RhB) and crystal violet (CV) through hydrogen bonding, π-π stacking, and electrostatic interactions. Individual and duplex detection of illicit food dyes (RhB and CV) was performed using TNRs@PDA/Ag to estimate SERS applications. Their linear equations and limits of detection of 1 nM for RhB and 5 nM for CV were derived. Individual and duplex food colour detection was successfully accomplished even in genuine chili meal with good results. The bifunctional TNRs@PDA/Ag-based highly sensitive and duplex SERS dye detection will have enormous potential for food safety monitoring.

1. Introduction

One of the most appealing and stunning features of foods that can draw customers' attention and influence their choice is food coloring [1,2]. Because of this, the use of food dyes has increased throughout time. Unfortunately, synthetic industrial dyes like rhodamine B (RhB) and crystal violet (CV), which have negative and toxic effects on human health, are frequently used illegally in the processing of chili products and cooked meat products due to their low cost, good stability, and strong coloring power [3,4]. Therefore, the management of food quality is related to the development of a sensitive, quick, and accurate method for numerous determinations of prohibited food dyes [5]. Surface-enhanced Raman scattering (SERS), one of many existing techniques, is acknowledged as a flexible analytical tool with speed, ultra-high sensitivity, and ease of use, making it potentially suitable for real-time and point-of-care analysis [6–8].

Designing and creating substrates with micro/nano architectures that produce SERS-active hotspots and maintain good stability and reproducibility is crucial for SERS applications [9–11]. Noble metal nanostructures, with their high enhancement factor (*EF*) and powerful local electromagnetic field are typically regarded as the most promising SERS substrates [12]. Pure metal nanostructures, however, typically have worse SERS repeatability and stability. Building semiconductor/noble metal heterostructures (such those made of TiO_2 and ZnO) is an effective way to address the limitations [13,14]. The most crucial concern for SERS applications is to design When the two of them are in the right energy level configuration, a suitable charge transfer path and a confined electromagnetic field are built to improve Raman scattering. The sensitivity and repeatability for SERS applications can be impressively increased, particularly for TiO_2 nanoarrays modified with noble metals [15–17]. For instance, rhodamine 6G was successfully detected using a graphene oxide/TiO_2 nanorod array (TNR) coated with Ag NPs, with a limit of detection (LOD) of 1 pM and a relative standard deviation (RSD) of less than 10 % [15]. Highly ordered TiO_2/Au nanotube arrays were investigated as a dependable SERS sensing platform for evaluating drugs for chronic myeloid leukemia [16]. However, pure TiO_2 has a wide bandgap (3.2 eV) and produces a high rate of electron-hole recombination. Combining complexes and TiO_2 to create heterojunction nanostructures is one effective method for reducing charge recombination because it allows for interfacial electron transport between the complexes and TiO_2 [18,19].

Due to its conjugated π structure, polydopamine (PDA), a biomimetic polymer, not only has good biocompatibility but also has a strong ability for light-harvesting [20]. The conjugated structure affords strong visible-light absorption, effective separation, and quick conveyance of photogenerated charge carriers [21–23]. These may be a result of the catalysts' ability to facilitate electron-hole separation by working in concert with PDA [22,23], on the other hand, is a multifunctional biopolymer that has significant quantities of aromatic, hydroxyl, and amine groups. Through interactions with hydrogen bonds and π-π stacking, the groups give aromatic dyes a PDA with high absorption capacity. We have previously described the sensitive and specific SERS detection of benzotriazole using the π-π PDA and benzotriazole [24]. By enhancing the absorption of deoxynivalenol through hydrogen bonding and π-π stacking interactions, Ag nanocubes with a thin PDA coating enabled the detection of deoxynivalenol at femtomolar levels in pig feed [25].

In this study, a novel TNRs@PDA/Ag film on FTO was constructed using PDA's structural properties, and it exhibits good SERS performance. One of the biomimetic PDAs served as an electron transfer mediator to improve the efficiency of electron transfer during the CT process, and the other served as an enrichment mediator to effectively enrich the illegal food dyes RhB and CV through hydrogen bonding, π-π stacking, and electrostatic interactions. It's significant to note that both dyes in chili meal were detected individually and simultaneously using SERS, enabling thorough monitoring of multiple dyes in food safety.

2. Experimental

2.1. Chemicals and materials

Silver nitrate ($AgNO_3$), L-ascorbic acid ($C_6H_8O_6$), ethanol, ethylene glycol and acetone were obtained from Sinopharm Chemical Reagent Co. Ltd. Titanium butoxide (TBOT), crystal violet (CV), rhodamine B (RhB), dopamine, tris(hydroxymethyl)methyl aminomethane ($C_4H_{11}NO_3$) and 4-mercaptobenzoic acid (4-MBA) were purchased from Shanghai Macklin Biochemical Co. Ltd. All chemicals were used as received unless specified. Deionized water of resistivity greater than 18.2 MΩ ▪ cm^{-1} was applied throughout the experiments. Fluorine-doped tin oxide (FTO) glass was purchased from Ao Pi Wei Te Company (Dalian, China). Rhodamine 6G (R6G) was purchased from Wenzhou Dongsheng Chemical Reagent Plant. Amoxicillin (AMO) was purchased from Macklin reagent. Congo red was purchased from Kermel.

2.2. Synthesis of the TNRs@PDA/Ag composites

In Scheme 1, the creation of the TNRs@PDA/Ag composites is depicted.

(1) The hydrothermal approach was used to create the TNRs on the FTO substrates [26]. First, acetone, ethanol, and water were individually ultrasonically washed with each FTO sheet. The round-bottomed flask was then filled with 30 mL of a 1:1 HCl solution, agitated for 5 min, and then filled with 0.5 mL of TBOBT. The mixture was then moved to a Teflon-lined stainless steel autoclave where the FTO sheets were positioned with the conductive side facing down and heated at 150 °C for 12 h after reacting for 5 min. The FTO sheets loaded with TNRs were removed and water cleaned.
(2) The TNRs@PDA was created using the following procedure: stirring while submerging the TNRs on FTO in a Tris-HCl solution (pH 8.5) containing dopamine (0.01 mg/mL). As a result, the TNRs were coated with an incredibly thin PDA layer before being rinsed in water. The polymerization duration was adjusted to control the PDA shell's thickness.
(3) The TNRs@PDA sheets were submerged in a 0.1 M $AgNO_3$ aqueous solution at 40 °C for 30 min to load the Ag NPs. The sheets were removed and left in a 40 °C, 0.1 M aqueous ascorbic acid solution for 30 min. The TNRs@PDA/Ag was then removed and thoroughly cleaned with water. By adjusting the concentration of $AgNO_3$, the amount of Ag decoration was managed.

$AgNO_3$ was present in this experiment at concentrations of 0.01, 0.05, 0.1, 0.2, or 0.5 M. To provide as a point of comparison, pristine TNRs were added to the reaction solution to create TNRs/Ag that did not have the PDA alteration.

Transmission electron microscopy (TEM, Tecnai G2 F30) and field emission scanning electron microscopy (FESEM, Hitachi, S-4800) were used to analyze the morphology of the TNRs@PDA/Ag. Using energy dispersive X-ray spectroscopy (EDX) and an aberration-corrected scanning transmission electron microscope (STEM), the elemental distribution of the samples was assessed. A drop of the sample solution was applied to copper grids to create the samples for TEM measurements. The crystalline structure was examined by X-ray powder diffraction (XRD, Rigaku D/max-2400, Cu Kα radiation $\lambda = 0.1541$ nm). A multipurpose X-ray photoelectron spectrometer (XPS, Thermo Scientific) with an Al Kα radiation source was used to determine the materials' composition. On a Cecil UV–vis–NIR 2021 spectrophotometer, UV–vis diffuse reflectance spectroscopy (DRS) was recorded between 300 and 800 nm. On a JASCO-FP-6500 spectrofluorimeter with a 150 W xenon lamp as the excitation light source at 265 nm, the photoluminescence (PL) spectra were taken.

Fluorescence measurements were made using an RF–5301 P C spectrofluorophotometer with a 355 nm excitation to gauge the capacity to quench fluorescence. Aqueous RhB (10 μM, 10 mL) solution was combined with TNRs or TNRs@PDA before to the measurement, which was given 10 min to complete.

2.3. SERS detection

Raman measurements were performed on a Raman spectrometer (Zolix Finder Vista-HiR). The following parameters were used to capture each Raman spectrum: 532 nm laser, 1.0 mW power, 1 μm diameter laser point, × 100 L objective, and 10 s collection duration. Optical focusing was made for each measurement. Each Raman spectrum was recorded using three successive observations.

RhB and CV were used as the probe molecules to assess the SERS performance of TNRs@PDA/Ag. The TNRs@PDA/Ag was immersed in 2 mL RhB or CV solutions with varying concentrations under static adsorption for 4 h before being exposed to SERS measurements on the dye-adsorbed TNRs@PDA/Ag. Individually, RhB and CV were detected utilizing their distinctive peaks, with the chosen concentrations falling between 10^{-5} to 10^{-9} M for RhB and between 10^{-5} to 5×10^{-9} M for CV. Simultaneous SERS determination was carried out since RhB and CV have independent characteristic peaks at 1653 cm^{-1} and 914 cm^{-1} and do not conflict with one another. After mixing the two dyes at the same concentration, which ranged from 10^{-5} to 10^{-8} M, the SERS measurements were carried out.

We bought chili sauce and powder at neighborhood grocers. Since garlic, ginger, sugar, and salt are also included in chili sauce, along with chili peppers and sesame oil, the pretreatment is required as follows: In 25 mL of methanol, 2.0 g of chili powder and chili sauce samples were added, and the mixture was vortex agitated for 3 min before being swirled in an ultrasonic bath for 10 min. Following centrifugation, the methanol extract was recovered and filtered once again using a 0.45 μm pore size filter. Finally, 50 times of the extract's volume was diluted with methanol. To calculate the recoveries, standard solutions of RhB and CV were added to the chili extract.

2.4. Computational setup

The following is a summary of the computational setup, which has frequently been discussed in the past [27–29] using a *Monte Carlo* simulation of annealing, RhB and CV were adsorbed onto PDA, respectively. A *Condensed-phase Optimized Molecular Potentials (COMPASS)* forcefield was employed in this study (for atomistic simulations). The CFF91, pcff (polymer consistent force field), CFF, and COMPASS (condensed-phase-optimized ab initio *force field*) are all members of the consistent family of forcefields. These second-generation forcefields include COMPASS, a new version of pcff that was parameterized against organic compounds containing halogen atoms and ions, alkali metal cations, as well as a number of divalent metal cations that are significant for biochemistry. So, for condensed phased complexes, COMPASS offers precise predictions of structural and thermophysical features [30].

Following the creation of three optimal positions for each of the two systems (PDA-RhB and PDA-CV) using the simulated annealing scheme, these positions were further geometrically and energetically optimized using calculations based on density functional theory. A Perdew-Wang (PW91) functional, which combines exchange and correlation functionals, was employed using a general gradient approximation. For 50 iterations, the convergence tolerance was 1.0×10^{-5} Ha. The valence electrons were described using the double-numeric-quality basic set with polarization functions basis set of DNP. After calculating the total energy ($E_{totalsystem}$), a single point energy calculation was used to obtain the binding energies (BEs) between the surfactants (E_s) and the NP (E_{np})):

$$E_b = (E_{totalsystem}) - E_{nanocluster} - E_{surfactant} \quad (1)$$

3. Results and discussion

3.1. Characterization of TNRs@PDA/Ag

A three-step technique that included the hydrothermal synthesis of TNRs, the self-polymerization of dopamine, and the chemical reduction of $AgNO_3$ with ascorbic acid (AA) was used to create the TNRs@PDA/Ag. The corresponding composition and morphology were described. TiO_2 nanorod arrays with good order and vertical alignment can be seen in the SEM picture (Fig. 1A). The nanorods (the inset of Fig. 1A) have a diameter of around 180 nm and a length of 1 μm. In spite of the PDA alteration from Fig. 1B, the shape of TNRs remains unchanged. The PDA shell, which has a thickness of around 4 nm on the surface of TNRs in the HRTEM image (Fig. 1C), is visible. The crystallographic facets of TiO_2 (002) fit nicely with the lattice fringes of d = 0.15 nm. According to the SEM image of the Ag NPs after additional loading, many tiny NPs are evenly distributed on the nanorods (Fig. 1D). The complete primary particle's homogeneous lattice fringes of TiO_2 and Ag can be seen from its HRTEM image (Fig. 1E). In the meantime, Ag (111) planes are represented by the lattice fringes of d = 0.24 nm [14]. The element

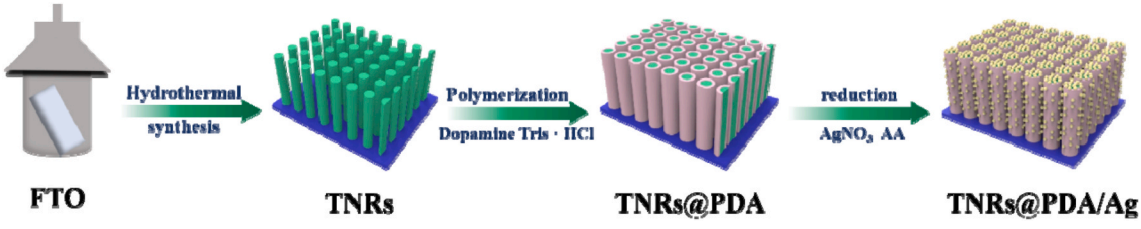

Scheme 1. Schematic diagram for the synthesis of TNRs@PDA/Ag.

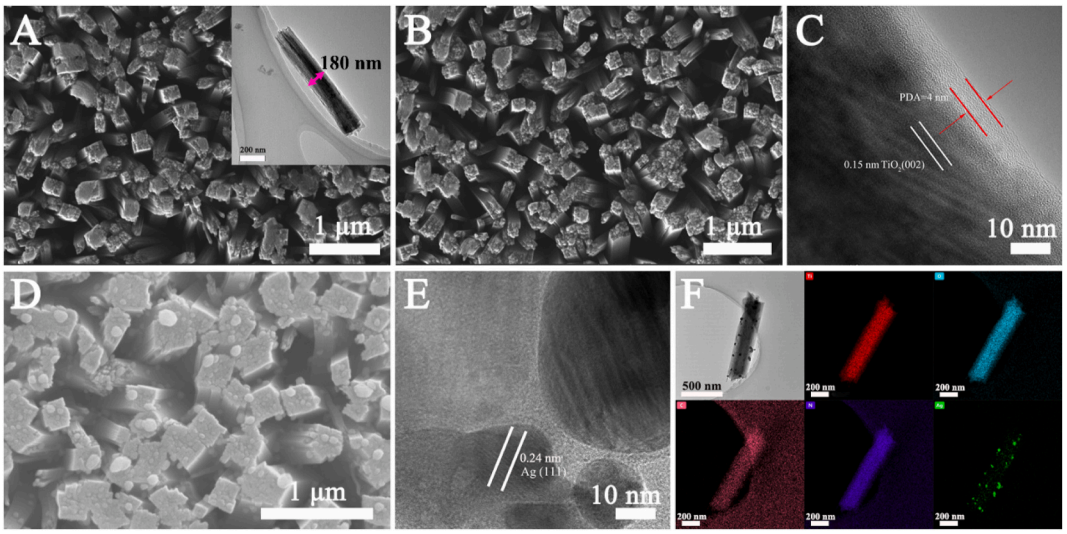

Fig. 1. SEM images of TNRs (A), TNRs@PDA (B) and TNRs@PDA/Ag (D). HRTEM images of TNRs@PDA (C) and TNRs@PDA/Ag (E). (F) EDX mapping of TNRs@PDA/Ag. The inset of (A) shows the TEM image of a single TNR.

dispersion was examined using the EDX element mapping. According to Fig. 1F, the elements C, N, O, Ti, and Ag show a uniform presence of PDA and TiO_2, with Ag dispersed throughout the nanorod.

XRD and Raman spectroscopy were used to further validate the production of TNRs@PDA/Ag. TNRs exhibit a rutile crystalline structure in Fig. 2A. Its diffraction peaks at 2θ are seen to be 36.2°, 41.5°, 62.9°, and 70.1°, and they are indexed to the crystal facets (101), (111), (002), and (112) (PDF no. 98-000-0081). The rutile TiO_2 diffraction peak positions in TNRs@PDA/Ag are identical to those in pristine TNRs. The interference of the FTO diffraction peaks and the low content make it challenging to differentiate Ag crystal planes in the XRD pattern. The bands associated with rutile TiO_2 for the two materials are located at 443 cm^{-1} and 608 cm^{-1} E_g) respectively, in the Raman spectra (Fig. 2B) [31]. The large peaks seen at 1582 cm^{-1} and 1354 cm^{-1} for TNRs@PDA and TNRs@PDA/Ag respectively demonstrate the creation of PDA, which corresponds to the stretching and deformation of aromatic rings [32]. The Ag EM effect, however, causes TNRs@PDA/Ag to have substantially higher Raman intensities than TNRs@PDA.

The surface chemical composition of TNRs, TNRs@PDA and TNRs@PDA/Ag was revealed by XPS. The XPS spectra of TNRs (Fig. S1) and TNRs@PDA (Fig. S2) are shown, where their corresponding element peaks can be clearly seen. For TNRs@PDA/Ag, the elements of C, O, N, Ti, and Ag in the survey spectrum are observed (Fig. 3A). Two Ag 3 d peaks in Fig. 3B, corresponding to Ag $3d_{5/2}$ and Ag $3d_{3/2}$, are located at 368.1 eV and 374.0 eV, respectively. In Fig. 3C, two distinct peaks for Ti $2p_{3/2}$ and Ti $2p_{1/2}$ (respectively) are seen. These peaks are indicative of Ti^{4+} in the composite and are located at 457.2 eV and 462.9 eV, respectively [33]. Peaks with the *C*–C/C═C (284.6 eV), *C*–N/C–O (284.2 eV), and C═O (282.3 eV) groups may be seen using peak fitting of C 1s (Fig. 3D). This gives support for the development of PDA. Pyrolic nitrogen (397.5 eV) and pyridinic nitrogen (391.6 eV) can be used to fit the N 1s spectrum (Fig. 3E). It alludes to the creation of PDA's indole unit [34]. Additionally, the *C*–O group and the binding of O atoms to titanium (Ti–O), respectively, are responsible for the O 1s peaks at 528.3 eV and 530.6 eV (Fig. 3F). The characterization results demonstrate that TNRs@PDA/Ag were successfully formed.

3.2. Study of the PDA role as an electron transfer mediator

The semiconductor-noble metal hybrids' SERS application heavily relies on the CT-induced amplification mechanism [13,14]. To enhance the CT impact in this work, PDA was added to the TNRs-Ag system. The probe molecule 4-MBA was chosen to make it easy to assess the P_{CT} (CT degree). The SERS spectra of 4-MBA (10^{-4} M) on TNRs@PDA/Ag and TNR/Ag are shown in Fig. 4A. The SERS intensity of TNRs@PDA/Ag is higher than that of TNR/Ag, as can be shown. The calibration is the intensity at 1585 cm^{-1}, and a 1.53-fold improvement is made.

The peak intensities at 1148 cm^{-1}, which are attributed to the b_2 vibration mode, and 1180 cm^{-1} which are allocated to the a_1 vibration mode, are used to determine the P_{CT} value. The Supporting Information

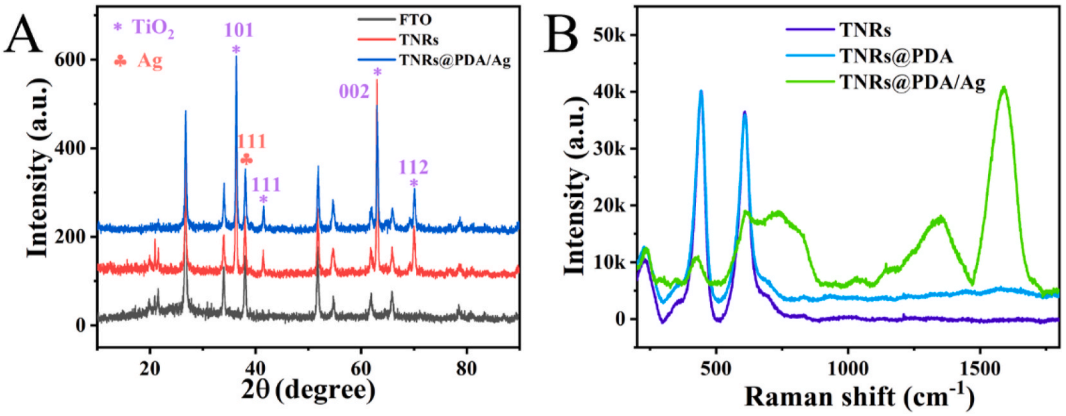

Fig. 2. (A) XRD patterns of FTO, TNRs, and TNRs@PDA/Ag. (B) Raman spectra of TNRs, TNRs@PDA, and TNRs@PDA/Ag.

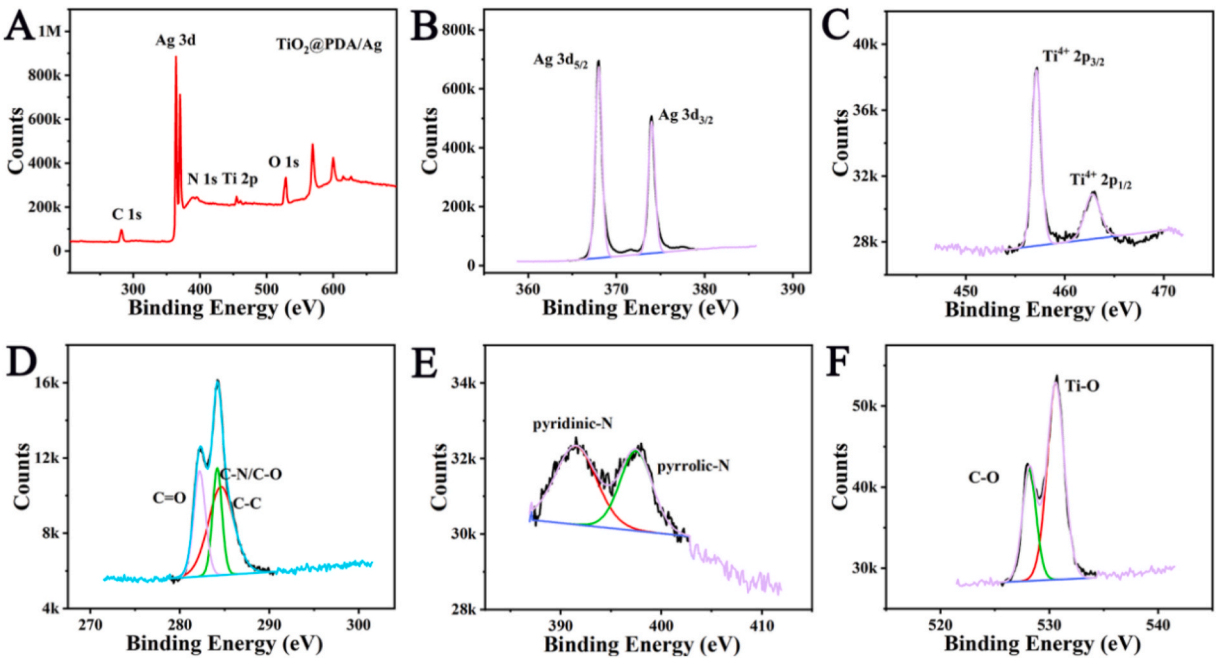

Fig. 3. XPS spectra of TNRs@PDA/Ag: survey spectrum (A), Ag 3 d (B), Ti 2p (C), C 1s (D), N 1s (E) and O 1s (F) spectra.

is a full breakdown of the computation procedure. In contrast to TNRs/Ag, where the value is just 0.18, the P_{CT} for TNRs@PDA/Ag is 0.24. Since Ag–S is easily formed, the SERS improvement isn't the result of 4-MBA adsorbing more readily to the PDA alteration [24]. Clearly, the 1.53-fold boost results from PDA's critical contribution to the CT-induced SERS enhancement.

Using 4-MBA as the probe molecule, the impact of Ag loading amount on the SERS activity was also assessed. Fig. S3 shows the SERS spectra of 4-MBA (10^{-4} M) absorbed on TNRs@PDA/Ag with varied growth concentrations of $AgNO_3$. Using the 1585 cm^{-1} peak as reference, the fluctuation of the peak intensity with the $AgNO_3$ concentration is depicted in Fig. 4B. The highest peak intensity is associated with a 0.1 M $AgNO_3$oncentration. When Harris et al. [35] used molecular dynamics simulations to examine the impact of the Ag NPs density in Ag–TiO_2 nanocomposites, they discovered that the highest SERS activity was correlated with a similar maximum Ag NPs density. Their justification claims that the phenomena is related to the surface plasmon resonance that results from the CT effect. The optimal Ag loading level with the maximum SERS intensity was directly correlated with the synergistic CT effect in our earlier Ag–ZnO system [36].

Additionally, the optical absorption characteristics of TNRs and TNRs@PDA were evaluated for the effectiveness of electron transmission. When PDA is wrapped around the surface of TNRs, as seen in the UV–vis DRS spectra (Fig. 4C), a stronger absorption intensity of TNRs@PDA exceeds in the visible-light region, indicating a significant increase in visible-light absorption and a greater suppression of the recombination of photo-generated charges [37]. The efficiency of charge-separation was demonstrated using PL spectra of TNRs and TNRs@PDA. A significant PL emission intensity is shown in Fig. 4D for pure TNRs, with the emission peak occurring at 612 nm. However, following the PDA adjustment, the intensity of the PL emission drops. It indicates that TNRs@PDA utilize visible light more than TNRs and have a lower recombination rate [38]. Using RhB as the probe molecule, the fluorescence quenching capacities of TNRs@PDA and TNRs were assessed. According to Fig. 4E, pristine TNRs has a low capacity to quench fluorescence. The intensity of the fluorescence peak still marginally reduces even after the addition of 50 μg/mL TNRs. TNRs@PDA, in contrast, exhibits significantly higher fluorescence quenching efficiency. The quenching efficiency increases to 82.2 % with the addition of 50 μg/mL TNRs@PDA (Fig. 4F). Energy and/or electron transport may be responsible for PDA's quenching effect [39]. The results mentioned above support the PDA modification's function as an electron transfer in the Ag–TiO_2 system.

Wang et al. [40] suggested a likely mechanism diagram for the CT process based on the TiO_2–Ag-Molecule system with regard to the CT-induced SERS augmentation. According to the process diagram (Fig. 5A), charges at the junction of Ag and TiO_2 are balanced and then transferred from Ag to the LUMO orbital of the probe molecules by the injection of electrons into the Fermi level (E_f) of Ag. Through the electron mediator of PDA, electrons gathered at the CB of TiO_2 are injected into the Fermi level (E_f) of Ag for the PDA modification, which results in a charge transfer and reorganization of their energy levels [41]. As a result, electrons can be injected into the molecules' LUMO with greater ease, leading to greater SERS amplification (Fig. 5B).

3.3. Study of the PDA role as an enrichment mediator

It is well known that PDA has a lot of amine, hydroxyl, and aromatic groups. Benzene rings and amine groups are features of the RhB and CV dyes. In order to effectively enrich the dyes, it allows for their absorption on PDA via π-π stacking and hydrogen bonding [42,43]. Using RhB and CV as the probe molecules, the SERS activities of TNRs/Ag and TNRs@PDA/Ag were compared on the basis of the concept. As anticipated, the Raman intensities of TNRs/Ag and TNRs@PDA/Ag for both dyes show clear distinctions. When referring to the typical peak (1653 cm^{-1}), TNRs@PDA/Ag has 4.3 times the peak intensity of TNRs/Ag for RhB detection (Fig. 6A). Similar to CV detection, TNRs@PDA/Ag and TNRs/Ag utilizing peak 914 cm^{-1} as the calibration have peak intensities that differ by approximately 2.7 times (Fig. 6B). When 4-MBA is used as the probe molecule, the peak intensity of TNRs@PDA/Ag is only 1.53 times that of TNRs/Ag (Fig. 4A). Ag–S is easily formed, hence 4-MBA is primarily bound to Ag sites. Therefore, there is little evidence of 4-MBA selective enrichment on TNRs@PDA/Ag or TNRs/Ag. For RhB and CV on Ag, physical adsorption is predominant. Of course, PDA's role as an enrichment mediator for RhB and CV is a significant contribution.

The DFT quantum mechanical approach was used to examine the interactions between PDA and RhB (or CV). From their optimum beginning positions, the three places with the lowest BEs, which indicate

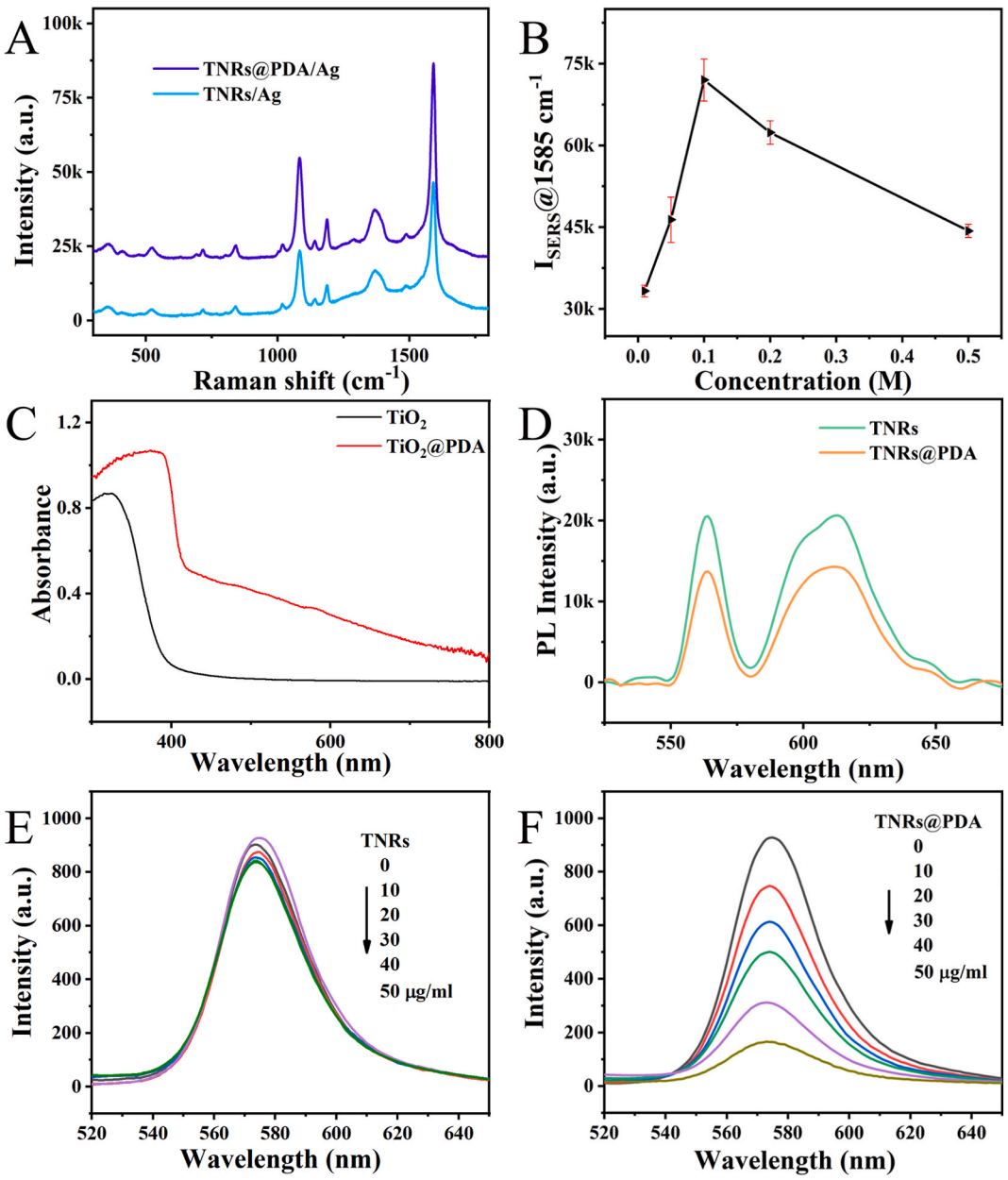

Fig. 4. (A) SERS spectra of different materials adsorbed with 10^{-4} M 4-MBA. (B) The corresponding peak intensity @1585 cm^{-1} of 4-MBA (10^{-4} M) with different $AgNO_3$ concentration. UV–vis DRS (C) and PL (D) spectra of TNRs and TNRs@PDA. Fluorescence spectra of 10 μM RhB after the addition of different amounts of TNRs (E) and TNRs@PDA (F).

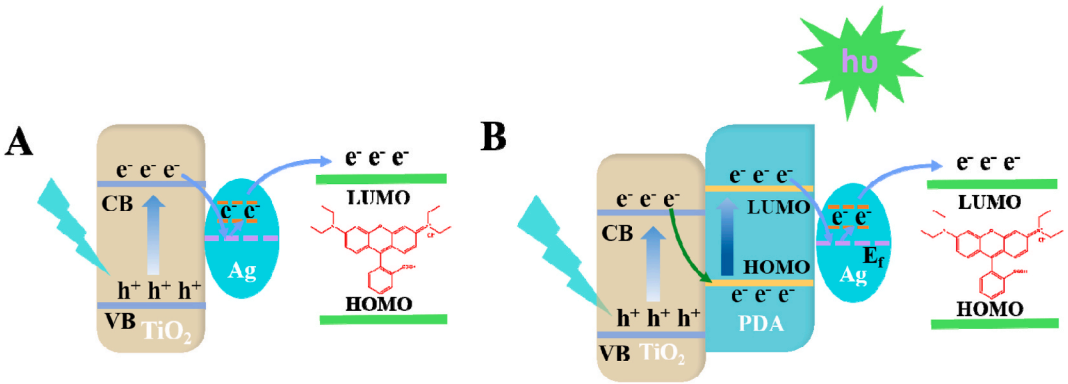

Fig. 5. The possible CT-induced enhancement progress in the TNRs/Ag–RhB (A) and TNRs@PDA/Ag–RhB (B) systems.

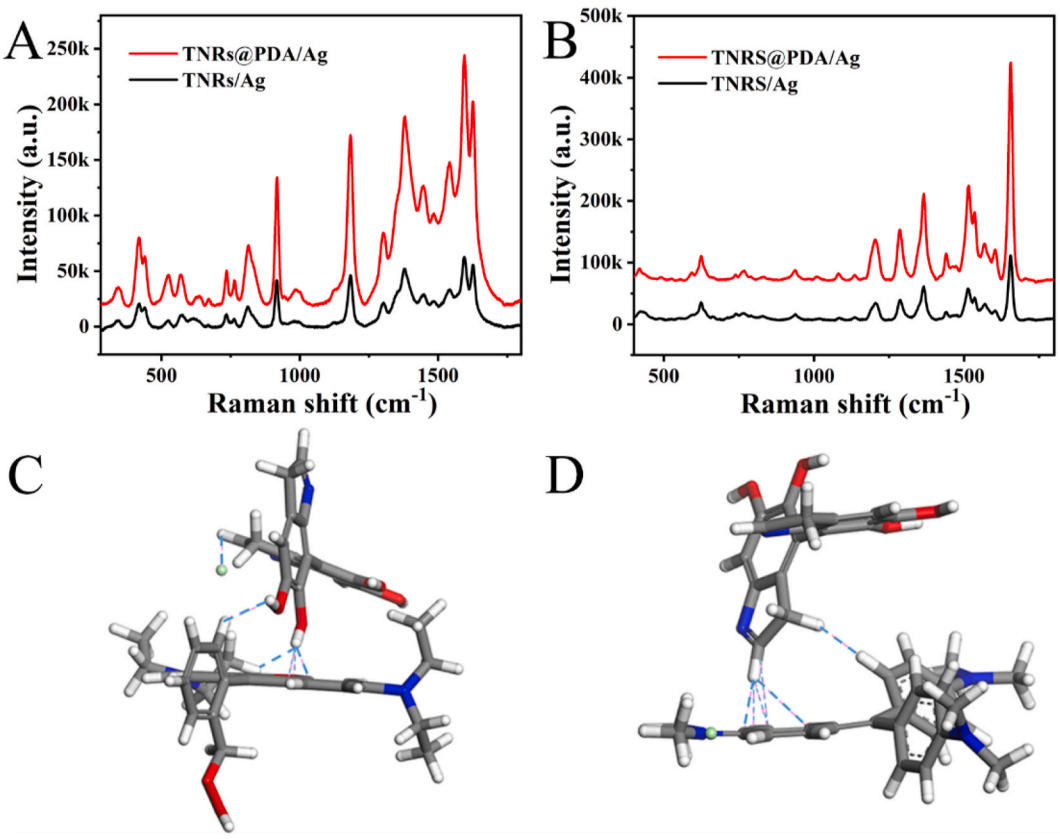

Fig. 6. SERS spectra of different materials adsorbed with RhB (A) and CV (B) of 10^{-5} M for each. DFT analysis of most likely positions of the dyes adsorbed onto PDA: about RhB for (C) the BE of −1.18 eV; about CV for (D) the BE of −1.63 eV. The blue lines indicate most probable hydrogen bonding sites. (For interpretation of the references to colour in this figure legend, the reader is referred to the Web version of this article.)

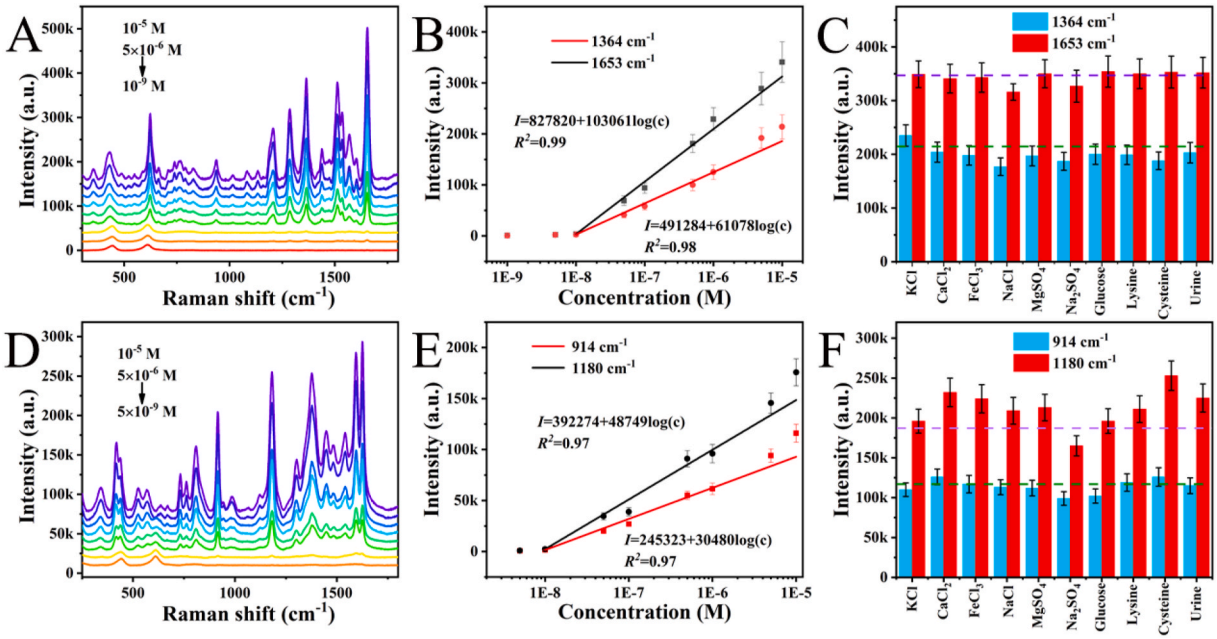

Fig. 7. SERS detection of RhB: (A) SERS spectra with different concentrations; (B) linear relationships between the concentration and the peak intensity@1364/1653 cm^{-1}; (C) anti-interference tests with 100-folds interfering substances compared with RhB. SERS detection of CV: (D) SERS spectra with different concentrations; (E) linear relationships between the concentration and the peak intensity@914/1180 cm^{-1}; (F) anti-interference tests with 100-folds interfering substances compared with RhB. Error bars indicate the standard deviation for five measurements.

the interactions, were chosen. These three configurations had corresponding BEs of (1) −0.29 eV, (2) −0.64 eV, and (3) −1.18 eV for the RhB-PDA systems (Fig. S5A). The BEs are also 2.97 eV, −0.29 eV, and −1.63 eV for the CV-PDA systems (Fig. S5B), respectively. The PDA-RhB and PDA-CV systems' most likely hydrogen bonding sites are, unsurprisingly, in Position 3. Furthermore, the direct stacking of aromatic rings during π-π stacking (also known as the "sandwich interaction") is electrostatically repellent. Either staggered stacking (parallel displaced) or π-teeing (perpendicular ant T-shaped) are the more frequent observations. Due to the near closeness of partially negatively charged carbon atoms and partially positively charged hydrogen atoms during π-teeing, the interactions of the two perpendicularly oriented rings are electrostatically attractive. The PDA alteration is advantageous to the SERS detection of RhB and CV through PDA interactions, according to the discussion above.

3.4. SERS detection of RhB and CV in chili food

3.4.1. Individual SERS detection

The SERS performances of TNRs@PDA/Ag were evaluated based on the merits of the binary mediators and included sensitivity, LOD, selectivity, uniformity, and repeatability. First, RhB was chosen as the analyte. RhB's SERS spectra at a range of concentrations (10^{-5} ~10^{-9} M) are shown in Fig. 7A. It is easy to identify the distinctive RhB Raman peaks, and Table S1 lists the peak assignments for each one. For instance, the stretching vibration of bridge *C*–C aromatic bonds and the stretching vibration of aromatic C═C are attributed to the usual peaks at 1364 cm^{-1} and 1653 cm^{-1}, respectively. As anticipated, the Raman peak intensities drop as the concentration decreases.

However, the distinctive peaks can still be seen at concentrations as low as 10^{-9} M. It is possible to get linear responses between the peak intensity and the logarithm of RhB concentration by using the typical peaks at 1364 $cm^{-1}$and 1653 cm^{-1} as the calibration (Fig. 7B), with a linear range of 10^{-5} to 10^{-8} M. The following is a list of the corresponding linear equations:

$$I = 491{,}284 + 61{,}078 \times \log(c_{RhB})\ R^2 = 0.98\ (1364\ cm^{-1}) \quad (2)$$

$$I = 827{,}820 + 103{,}061 \times \log(c_{RhB})\ R^2 = 0.99\ (1653\ cm^{-1}) \quad (3)$$

The LOD for RhB detection is 1 nM based on a signal-to-noise (S/N) ratio of 3. The majority of materials (including pure Ag nanowires) and techniques such immunoassay, UV–Vis spectrophotometry, fluorescence, electrochemistry, and SERS are inferior to or compatible with this detection capability in the LOD and linear range (Table S2). Ozkantar et al. [44] reported a sensitive UV–Vis spectrophotometry with the LOD of 1 nM, however, the method required a challenging dispersive liquid-liquid microextraction approach for the separation and preconcentration of RhB. The *EF* was estimated in accordance with Table S4 and the supporting information. The distinctive peaks at 1364 and 1653 cm^{-1} have corresponding *EFs* of 1.6×10^6 and 1.3×10^6.

The analyte on the TNRs@PDA/Ag was likewise chosen to be another aromatic dye (CV). Similar CV Raman peaks can be seen in Fig. 7D, SERS spectra for the same compounds at various doses (10^{-5}–5×10^{-9} M). The peaks are categorized as shown in Table S1. The aromatic ring breathing and the aromatic *C*–H in-plane antisymmetric stretching are related to the peaks at 914 and 1180 cm^{-1}, respectively. Peak intensities (914 and 1180 cm^{-1}) are obtained as linear curves from 10^{-5} to 10^{-8} M (Fig. 7E) against the logarithm of CV concentration. The following is a list of the linear equations:

$$I = 345{,}323 + 30{,}480 \times \log(c_{CV})\ R^2 = 0.97\ (914\ cm^{-1}) \quad (4)$$

$$I = 392{,}274 + 48{,}749 \times \log(c_{CV})\ R^2 = 0.97\ (1180\ cm^{-1}) \quad (5)$$

From a S/N of 3, the LOD for CV detection is 1 nM. According to Table S3, the LOD of the TNRs@PDA/Ag probe is less severe than or comparable to other earlier detection techniques, including HPLC, fluorescence, and SERS. A few powder materials, including Ag-encapsulated Fe@SiO_2 [45] and boron nitride/gold [46] exhibited lower LODs than this substance. On the other hand, this substance displayed a nanoarray structure on FTO that made it simple to provide uniformity and convenience in SERS detection. At 914 cm^{-1} and 1180 cm^{-1}, the computed *EFs* are 1.2×10^6 and 1.65×10^6, respectively (Table S4).

For the two dyes, uniformity and reproducibility were assessed, including batch-to-batch repeatability as well as point-to-point and spot-to-spot uniformity. Supporting Information and Figs. S6–S9 contain a full analysis. For either a high concentration (10^{-5} M) or a low concentration (10^{-7} M), all of the relative standard deviations (RSDs) are less than 10 %, showing good uniformity and reproducibility. Additionally, the stability was determined by contrasting the SERS intensities of the probe before and after it was kept in air for a week. Fig. S10A displays the SERS spectra using CV as the probe molecule. The attenuation rates toward the peak intensities are estimated to be less than 20 % for the CV peaks at 914 and 1180 cm^{-1} (Fig. S10B).

Additionally, the addition of these interfering species with 100-fold dye concentrations allowed access to the detection selectivity. Fig. 7C and F shows that their typical peak intensities only fluctuate by less than 15 % when compared to the control solution. The findings demonstrate that the TNRs@PDA/Ag probe can successfully detect RhB and CV using SERS in actual samples.

The aforementioned linear equations were used to individually identify the colours included in chili powder and sauce purchased from local markets. Their components were not discovered in actual samples. The standard addition method was additionally used by individually injecting RhB and CV with the known concentrations into the real samples to calculate the recoveries. This was done to confirm the validity of this detect method. To assess the RSD, five parallel trials were run under identical circumstances. The contents of RhB and CV were determined using the linear equations corresponding to their two Raman peaks, as shown in Tables S5 and S6. With the exception of a few recoveries of around 85 %, the majority range from 90 % to 105 % and are satisfactory. The fact that all RSDs are capped at 10 % is encouraging. The TNRs@PDA/Ag probe's suitability for sensitive and quick monitoring of RhB and CV in chili-based foods is confirmed by good recoveries and RSDs.

Based on the TNRs@PDA/Ag probe, additional compounds such as R6G, AMO, Congo red, and 4-MBA were also successfully detected. Even at their nanomolar concentrations, high distinctive Raman peaks with good band resolution can be readily seen in Fig. S13.

3.4.2. Simultaneous SERS measurement

Using a single detection substrate allows for rapid, straightforward, and cost-effective duplex detection of dyes like RhB and CV. Here, the specific peak intensities at 1653 cm^{-1} for RhB and 914 cm^{-1} for CV can be used to detect RhB and CV in duplex SERS.

The SERS spectra of the RhB and CV mixed solution, with concentrations ranging from 10^{-5} to 10^{-8} M are shown in Fig. 8A. Linear detection curves are produced using their unique distinctive peak intensities (Fig. 8B). The linear range is 10^{-5} to 10^{-7} M, and the following are the linear regression equations:

$$I = 588{,}526 + 76{,}936 \times \log(c_{RhB})\ R^2 = 0.98\ (1653\ cm^{-1}) \quad (6)$$

$$I = 252{,}408 + 32{,}558 \times \log(c_{CV})\ R^2 = 0.97\ (914\ cm^{-1}) \quad (7)$$

The RhB and CV solutions with defined concentrations were combined with chili sauce and powder using the conventional addition method. The TNRs@PDA/Ag probe was used to incubate the samples, and the results are shown in Figs. S11 and S12. Their concentrations can be determined from their individual peak intensities using Eqs. (6) and (7). Table 1 contains a list of the recoveries and RSDs. The recoveries range from 88.3 % to 101.5 % and the RSDs are less than 8 % for three spiked concentrations (1×10^{-5}, 1×10^{-6} and 1×10^{-7} M) in two

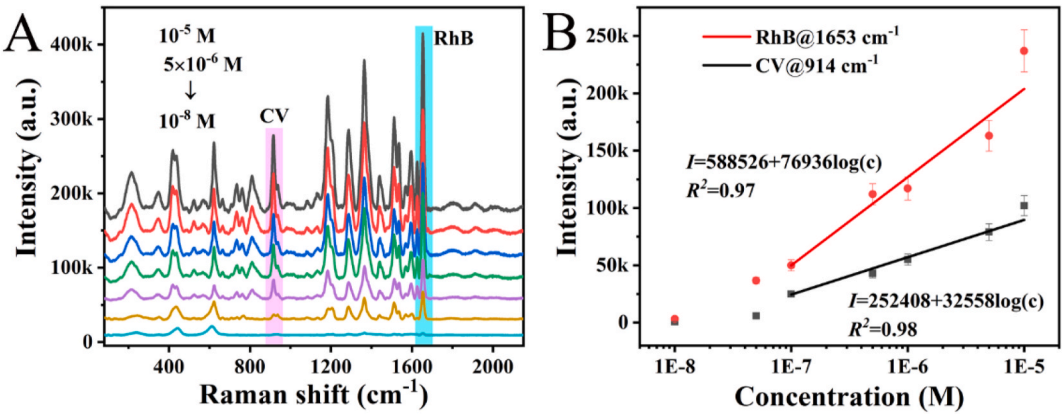

Fig. 8. (A) SERS spectra of simultaneous detection of RhB and CV at the same concentration. (B) The linear relationship between the concentration and the peak intensity.

Table 1
Simultaneous SERS detection of RhB and CV mixed in chili food.

Analyte	Raman peak (cm^{-1})	Spiked (M)	Recovery (%)	RSD (%)
RhB (chili powder)	1653	1×10^{-5}	90.34	7.07
		1×10^{-6}	95.63	3.46
		1×10^{-7}	98.58	2.51
RhB (chili sauce)		1×10^{-5}	91.48	4.40
		1×10^{-6}	98.43	3.89
		1×10^{-7}	101.5	0.79
CV (chili powder)	914	1×10^{-5}	89.81	5.69
		1×10^{-6}	99.82	1.34
		1×10^{-7}	99.75	0.36
CV (chili sauce)		1×10^{-5}	88.30	6.97
		1×10^{-6}	100.9	4.02
		1×10^{-7}	101.5	1.10

varieties of chili cuisine. Clearly, despite the complex ingredients in chili meals, the recoveries and RSDs are pretty satisfactory.

4. Conclusions

To serve as the SERS substrate, the TNRs@PDA/Ag is simply produced, and the morphology and content are rigorously studied. Through hydrogen bonds, π-π stacking, and electrostatic interactions, the PDA alteration in the structure serves as binary mediators for the electron transfer and effective enrichment toward illicit food dyes (RhB and CV). The TNRs@PDA/Ag displays exceptional SERS characteristics based on these, including high sensitivity, homogeneity, and reproducibility. Chili food containing RhB and CV has been successfully detected using individual and duplex SERS methods with acceptable recoveries and RSDs. The TNRs@PDA/Ag is anticipated to be a notable SERS substrate for the potential applications in regular food quality control, as shown by the duplex detection capability and real-sample analysis.

CRediT authorship contribution statement

Lin Tan: Conceptualization, Investigation, Visualization, Writing – original draft. **Yanqiang Cao:** Conceptualization, Investigation, Visualization, Writing – original draft. **Juanjuan Yan:** Investigation, Visualization, Writing – original draft. **Kang Mao:** Visualization. **Li Liu:** Resources, Visualization. **Xiaolong Wang:** Resources, Writing – review & editing. **Weichun Ye:** Conceptualization, Writing – original draft, Writing – review & editing, Project administration, Supervision. **R.A. Harris:** DFT caculation, Writing – review & editing. **Hua Zhang:** Resources, Writing – review & editing, All authors have read and agreed to the published version of the manuscript.

Declaration of competing interest

The authors declare that they have no known competing financial interests or personal relationships that could have appeared to influence the work reported in this paper.

Data availability

No data was used for the research described in the article.

Acknowledgment

This work is supported by the Fundamental Research Funds for the National Key Research and Development Project (No.2020YFC1807301), Natural Science Foundation of Gansu Province, China (No.21JR7RA463), National Natural Science Foundation of China (No.42107486), the State Key Laboratory of Environmental Geochemistry (No.SKLEG2022209), the Fundamental Research Funds for the Central Universities (No. lzujbky-2022-kb01), the Science and Technology Projects of Gansu Drug Administration (No. 2022GSMPA009; 2022GSMPA0036) , the project of Gansu Traditional Chinese Medicine Industry Innovation Association (No. 22ZD6FA021).

Appendix A. Supplementary data

Supplementary data to this article can be found online at https://doi.org/10.1016/j.aca.2023.342047.

References

[1] N. Bhargava, V.S. Sharanagat, R.S. Mor, K. Kumar, Active and intelligent biodegradable packaging films using food and food waste-derived bioactive compounds: a review, Trends Food Sci. Technol. 105 (2020) 385–401.
[2] V. Katheresan, J. Kansedo, S.Y. Lau, Efficiency of various recent wastewater dye removal methods: a review, J. Environ. Chem. Eng. 6 (2018) 4676–4697.
[3] Y.Y. Cheng, T.H. Tsai, Pharmacokinetics and biodistribution of the illegal food colorant rhodamine B in rats, J. Agric. Food Chem. 65 (2017) 1078–1085.
[4] J. Yang, Y. Zhang, S. Wang, S. Li, Y. Wang, S. Wang, H. Li, Biodegradation of crystal violet mediated by CotA from Bacillus amyloliquefaciens, J. Biosci. Bioeng. 130 (2020) 347–351.
[5] M. Dong, H. Wu, W. Long, T. Wang, R. Yu, Simultaneous and rapid screening and determination of twelve azo dyes illegally added into food products by using chemometrics-assisted HPLC-DAD strategy, Microchem. J. 171 (2021), 106775.
[6] L. Wang, X. Wang, L. Cheng, S. Ding, G. Wang, J. Choo, L. Chen, SERS-based test strips: principles, designs and applications, Biosens. Bioelectron. 189 (2021), 113360.
[7] X. He, S. Yang, T. Xu, Y. Song, X. Zhang, Microdroplet-captured tapes for rapid samplinh and SERS detection of food contaminants, Biosens. Bioelectron. 152 (2020), 112013.
[8] Y. Hang, J. Boryczka, N. Wu, Visible-light and near-infrared fluorescence and surface-enhanced Raman scattering point-of-care sensing and bio-imaging: a review, Chem. Soc. Rev. 51 (2022) 329–375.

[9] H.K. Lee, Y.H. Lee, C.S.L. Koh, C.P.Q. Gia, X. Han, C.L. Lay, H.Y.F. Sim, Y. Kao, Q. An, X.Y. Ling, Designing surface-enhanced Raman scattering (SERS) platforms beyond hotspot engineering: emerging opportunities in analyte manipulations and hybrid materials, Chem. Soc. Rev. 48 (2019) 731–756.
[10] J. Xiao, J. Wang, Y. Luo, T. Xu, X. Zhang, Wearable plasmonic swear biosensor for acetaminophen drug monitoring, ACS Sens. 8 (2023) 1766–1773.
[11] X. He, C. Fan, Y. Luo, T. Xu, X. Zhang, Flexible microfluidic nanoplasmonic sensors for refreshable and portable recognition of sweat biochemical fingerprint, npj Flex. Electron. 6 (2022) 60.
[12] X. Wang, S. Huang, S. Hu, S. Yan, B. Ren, Fundamental understanding and applications of plasmon-enhanced Raman spectroscopy, Nat. Rev. Phys. 2 (2020) 253–271.
[13] Y. Wang, J. Liu, Y. Ozaki, Z. Xu, B. Zhao, Effect of TiO_2 on altering direction of interfacial charge transfer in a TiO_2-Ag-MPY-FePc system by SERS, Angew. Chem.-Int. Edit. 58 (2019) 8172–8176.
[14] C. Wang, X. Xu, G. Qiu, W. Ye, Y. Li, R.A. Harris, C. Jiang, Group-targeting SERS screening of total benzodiazepines based on large-size (111) faceted silver nanosheets decorated with zinc oxide nanoparticles, Anal. Chem. 93 (2021) 3403–3410.
[15] Y. Wang, M. Zhang, H. Yu, Y. Zuo, J. Gao, G. He, Z. Sun, Facile fabrication of Ag/graphene oxide/TiO_2 nanorod array as a powerful substrate for photocatalytic degradation and surface-enhanced Raman scattering detection, Appl. Catal. B Environ. 252 (2019) 174–186.
[16] S. Wen, Y. Su, R. Wu, S. Zhou, Q. Min, G. Fan, L. Jiang, R. Song, J. Zhu, Plasmonic Au nanostar Raman probes coupling with highly ordered TiO_2/Au nanotube arrays as the reliable SERS sensing platform for chronic myeloid leukemia drug evaluation, Biosens. Bioelectron. 117 (2018) 260–266.
[17] H. Fang, C.X. Zhang, L. Liu, Y.M. Zhao, H.J. Xu, Recyclable three-dimensional Ag nanoparticle-decorated TiO_2 nanorod arrays for surface-enhanced Raman scattering, Biosens. Bioelectron. 64 (2015) 434–441.
[18] M.S. Kim, H.Y. Yoo, G.E. Choi, S. Jo, H. Shin, J. Lim, Visible light photocatalysis of TiO_2 complexed with albumin via a ligand-to-metal charge transfer (LMCT) pathway, J. Phys. Chem. C 127 (2023) 5408–5415.
[19] G. Zhang, G. Kim, W. Choi, Visible light driven photocatalysis mediated via ligand-to-metal charge transfer (LMCT): an alternative approach to solar activation of titania, Energy Envion. Sci. 7 (2014) 954–966.
[20] H. Lee, S.M. Dellatore, W.M. Miller, P.B. Messersmith, Mussel-inspired surface chemistry for multifunctional coatings, Science 318 (2007) 426–430.
[21] M. Lee, J.U. Kim, K.J. Lee, S. Ahn, Y.B. Shin, J. Shin, C.B. Park, Aluminum nano arrays for plasmon-enhanced light harvesting, ACS Nano 9 (2015) 6206–6213.
[22] X. Zhou, B. Jin, J. Luo, X. Gu, S. Zhang, Photoreduction preparation of Cu_2O@polydopamine nanospheres with enhanced photocatalytic activity under visible light irradiation, J. Solid State Chem. 254 (2017) 55–61.
[23] X. Zhou, B. Jin, J. Luo, X. Xu, L. Zhang, J. Li, H. Guan, Dramatic visible light photocatalytic degradation due to the synergetic effects of TiO_2 and PDA nanospheres, RSC Adv. 6 (2016) 64446–64449.
[24] W. Ye, H. Huang, W. Yang, X. Wang, C. Ren, Q. Hu, Y. Li, B. Ren, Ultrathin polydopamine film coated gold nanoparticles: a sensitive, uniform, and stable SHINERS substrate for detection of benzotriazole, Analyst 142 (2017) 3459–3467.
[25] W.A. Tegegne, M.L. Mekonnen, A.B. Beyene, W.N. Su, B. Joe Hwang, Sensitive and reliable detection of deoxynivalenol mycotoxin in pig feed by surface enhanced Raman spectroscopy on silver nanocubes@polydopamine substrate, Spectroc. Acta Pt. A-Molec. Biomolec. Spectr. 229 (2020), 117940.
[26] B. Liu, E.S. Aydil, Growth of oriented single-crystalline rutile TiO_2 nanorods on transparent conducting substrates for dye-sensitized solar cells, J. Am. Chem. Soc. 131 (2009) 3985–3990.
[27] A.S.H. Nasr, H. Akbarzadeh, R. Tayebee, Adsorption mechanism of different acyclovir concentrations on 1-2 nm sized magnetite nanoparticles: a molecular dynamics study, J. Mol. Liq. 254 (2018) 64–69.
[28] R.A. Harris, Chemotherapy drug temozolomide adsorbed onto iron-oxide (Fe_3O_4) nanoparticles as nanocarrier: a simulation study, J. Mol. Liq. 288 (2019), 111084.
[29] R.A. Harris, P.M. Shumbula, H. van der Walt, Analysis of the interaction of surfactants oleic acid and oleylamine with iron oxide nanoparticles through molecular mechanics modeling, Langmuir 31 (2015) 3934–3943.
[30] R.A. Harris, J. Prakash, Surface enhanced Raman scattering with methyl-orange on Ag-TiO_2 nanocomposites: a computational investigation, J. Mol. Graph. 87 (2019) 220–226.
[31] C. Li, M. Gu, M. Gao, K. Liu, X. Zhao, N. Cao, J. Feng, Y. Ren, T. Wei, M. Zhang, N-doping TiO_2 hollow microspheres with abundant oxygen vacancies for highly photocatalytic nitrogen fixation, J. Colloid Interface Sci. 609 (2022) 341–352.
[32] W. Ye, D. Wang, H. Zhang, F. Zhou, W. Liu, Electrochemical growth of flowerlike gold nanoparticles on polydopamine modified ITO glass for SERS application, Electrochim. Acta 55 (2010) 2004–2009.
[33] F. Chen, W. Yu, Y. Qie, L. Zhao, H. Zhang, L. Guo, Enhanced photocatalytic removal of hexavalent chromium through localized electrons in polydopamine-modified TiO_2 under visible irradiation, Chem. Eng. J. 373 (2019) 58–67.
[34] X. Zhou, B. Jin, J. Luo, X. Gu, S. Zhang, Photoreduction preparation of Cu_2O@polydopamine nanospheres with enhanced photocatalytic activity under visible light irradiation, J. Solid State Chem. 254 (2017) 55–61.
[35] R.A. Harris, J. Prakash, Surface enhanced Raman scattering with methyl-orange on Ag-TiO_2 nanocomposites: a computational investigation, J. Mol. Graph. 87 (2019) 220–226.
[36] C. Liu, X. Xu, C. Wang, G. Qiu, W. Ye, Y. Li, D. Wang, ZnO/Ag nanorods as a prominent SERS substrate contributed by synergistic charge transfer effect for simultaneous detection of oral antidiabetic drugs pioglitazone and phenformin, Sensor. Actuator. B Chem. 307 (2020), 127634.
[37] W. Qiang, W. Li, X. Li, X. Chen, D. Xu, Bioinspired polydopamine nanospheres: a superquencher for fluorescence sensing of biomolecules, Chem. Sci. 5 (2014) 3018–3024.
[38] F. Chen, W. Yu, Y. Qie, L. Zhao, H. Zhang, L. Guo, Enhanced photocatalytic removal of hexavalent chromium through localized electrons in polydopamine-modified TiO_2 under visible irradiation, Chem. Eng. J. 373 (2019) 58–67.
[39] X. Zhou, B. Jin, J. Luo, X. Gu, S. Zhang, Photoreduction preparation of Cu_2O@polydopamine nanospheres with enhanced photocatalytic activity under visible light irradiation, J. Solid State Chem. 254 (2017) 55–61.
[40] Y. Wang, J. Liu, X. Zhao, C. Yang, Y. Ozaki, Z. Xu, B. Zhao, Z. Yu, A chiral signal-amplified sensor for enantioselective discrimination of amino acids based on charge transfer-induced SERS, Chem. Commun. 55 (2019) 9697–9700.
[41] A. Meng, B. Cheng, H. Tan, J. Fan, C. Su, J. Yu, TiO_2/polydopamine S-scheme heterojunction photocatalyst with enhanced CO_2-reduction selectivity, Appl. Catal. B Environ. 289 (2021), 120039.
[42] J. Wang, Y. Yang, H. Li, J. Gao, P. He, L. Bian, F. Dong, Y. He, Stable and tunable plasmon resonance of molybdenum oxide nanosheets from the ultraviolet to the near-infrared region for ultrasensitive surface-enhanced Raman analysis, Chem. Sci. 10 (2019) 6330–6335.
[43] M. Zhang, L. Li, B. Li, N. Tian, M. Yang, H. Zhang, C. You, J. Zhang, Adsorption of DNA by using polydopamine modified magnetic nanoparticles based on solid-phase extraction, Anal. Biochem. 579 (2019) 9–17.
[44] N. Ozkantar, M. Soylak, M. Tüzen, Spectrophotometric detection of rhodamine B in tap water, lipstick, rouge, and nail polish samples after supramolecular solvent microextraction, Turk. J. Chem. 41 (2017) 987–994.
[45] S. Senapati, S.K. Srivastava, S.B. Singh, A.R. Kulkarni, SERS active Ag encapsulated Fe@SiO_2 nanorods in electromagnetic wave absorption and crystal violet detection, Environ. Res. 135 (2014) 95–104.
[46] H. Zhang, G. Li, S. Li, L. Xu, Y. Tian, A. Jiao, X. Liu, F. Chen, M. Chen, Boron nitride/gold nanocomposites for crystal violet and creatinine detection by surface-enhanced Raman spectroscopy, Appl. Surf. Sci. 457 (2018) 684–694.